Health diagnosis and recuperation of aged Li-ion batteries with data analytics and equivalent circuit modeling

Riko I Made,[1] Jing Lin,[2] Jintao Zhang,[1] Yu Zhang,[2] Lionel C. H. Moh,[1] Zhaolin Liu,[1] Ning Ding,[1] Sing Yang Chiam,[1] Edwin Khoo,[2,*] Xuesong Yin[1,4,*] and Guangyuan Wesley Zheng[3,*]

[1] Institute of Materials Research and Engineering (IMRE), Agency for Science, Technology and Research (A*STAR), 2 Fusionopolis Way, Innovis #08-03, Singapore 138634, Republic of Singapore.

[2] Institute for Infocomm Research (I^{2}R), Agency for Science, Technology and Research (A*STAR), 1 Fusionopolis Way, #21-01 Connexis, Singapore 138632, Republic of Singapore.

[3] Posh Robotics, 3501 Breakwater Court, Hayward, CA 94545, United States.

[4] Lead contact

[*]Correspondence: yinxs@imre.a-star.edu.sg, edwin_khoo@i2r.a-star.edu.sg and wesley@poshrobotics.com

SUMMARY

Battery health assessment and recuperation play crucial roles in the utilization of second-life Li-ion batteries. However, due to ambiguous aging mechanisms, it is challenging to estimate battery health and devise an effective strategy for cell rejuvenation. This paper presents aging and reconditioning experiments of 62 commercial lithium iron phosphate cells, which allow us to use machine learning models to predict cycle life and identify important indicators of recoverable capacity. An average test error of 16.84% ± 1.87% (mean absolute percentage error) for cycle life prediction is achieved by gradient boosting regressor. Some of the recoverable lost capacity is found to be attributed to the non-uniformity in electrodes. An experimentally validated equivalent circuit model is built to demonstrate how such non-uniformity can be accumulated, and how it can give rise to recoverable capacity loss. Furthermore, SHapley Additive exPlanations (SHAP) analysis also reveals that battery operation history significantly affects the capacity recovery.

INTRODUCTION

Large numbers of Li-ion batteries (LIBs) are produced to meet the ever-growing demands of the electric vehicle (EV) market up to an annual capacity of 2500 GWh by 2030.[1] These EV batteries will eventually retire and accumulate after their service due to a limited cycle life.[2] The precious and hazardous nature of LIB components necessitates materials recycling to attain a sustainable battery industry and circular economy.[3-8] Meanwhile, considerable residual capacities after EV applications, normally above 70% of the initial capacities, bring about an emerging field of repurposing and remanufacturing of retired EV batteries for less demanding applications, like low-speed vehicles or energy storage systems.[9,10] Therefore, providing a second life to retired batteries becomes an economically viable method to extend their service life before materials recycling (Figure 1).

State of health (SoH), which is defined by the ratio of residual to initial capacity ($\mathrm{SoH} = C_{res}/C_{ini}$) and describes the aging status, is an essential parameter to be understood before any repurposing activities.[11-13] However, the ambiguous aging mechanisms of Li-ion batteries make it challenging to estimate SoH accurately.[14] Data-driven methodologies show great potential in dealing with complex systems with non-linear behaviors. Severson et al. (2019) collected a big dataset of 142 commercial LFP cells and developed a machine learning approach for early prediction of cycle life.[15] Roman et al. (2021) explored four different machine learning algorithms and correlated the prediction accuracies with charging protocols.[16] Li et al. (2021) developed an online capacity estimation model with recurrent neural networks for cells operated in real-world.[17] Aitio et al. (2021) used battery data from real-world off-grid solar-battery systems to analyze health and end-of-life failure through machine learning.[18] Takahashi et al. (2023) presented a combination of machine learning techniques to evaluate retired EV batteries.[19] Xu et al. (2023) applied a hybrid deep learning approach to achieve early prediction of remaining useful life of EV batteries.[20] In addition to Li-ion batteries, Ma et al. (2023) reported prediction of remaining useful life for supercapacitors by improved long short-term memory recurrent neural networks.[21] Cell chemistries and operational conditions, such as formation, charge/discharge currents, cut-off voltages, depth of discharge and temperature, have been considered in generating datasets.[22-24] Nevertheless, the intrinsic inconsistencies in cell performance that result from the imperfection of cell manufacturing are often overlooked by assuming the cells of the same batch or manufacturer are identical. In practice, even batteries from the same batch will have different SoHs when used in a battery pack, because individual cells in a pack rarely work under an ideally equivalent operational or environmental condition.[25] For second-life batteries, this inconsistency problem becomes more significant when various cells with different operational histories need to be re-grouped and employed in a new system. Therefore, cell consistency is an important factor to examine when assessing the SoH of Li-ion batteries.

In addition to an accurate estimation of the SoH, it is also beneficial to recuperate some lost capacity of the retired cells before a second-life application. This task is also highly dependent on the aging mechanisms. Various and mixed degradation modes have been proposed to understand the aging behaviors of Li-ion batteries,[12,26-28] but only those involving reversible changes may contribute to a capacity recovery.

Electrolyte consumption has been considered as an aging factor, and Cui et al. (2016) reported re-filling electrolyte was able to achieve a capacity recovery over 10%.[29] Direct lithiation from an external lithium source was also proven effective to compensate lost Li inventory in the cathode and recover some capacity by Wang et al. (2011) and Taniyama et al. (2016).[30,31] However, the invasive nature of these methods posts challenges towards a large-scale and reliable process that can be readily adopted by industry. For non-invasive methods, thermal treatment was proposed to break and re-build the solid-electrolyte interface (SEI) layer, whose continuous growth during cycling was believed to be the reason for loss of active Li and increase of cell impedance.[32] Waldmann et al. (2017) reported a capacity recovery behavior by resting commercial cells in different temperatures.[33] To partially reverse degradation attributed to a non-uniform distribution of Li ions, extreme voltage reconditioning was proposed to re-distribute and activate the inactive Li ions by Hall et al. (2006) and Springer et al. (2020).[34,35] Although discrete trials on individual cells were reported, there lacks a comprehensive evaluation of the effectiveness of cell capacity recovery techniques with a sufficient sampling quantity where the cell inconsistency is considered.

Lithium iron phosphate (LFP) batteries are a popular candidate in various energy storage applications because of its long cycle life, high safety and low cost.[36] The relatively low value of the raw materials makes recycling of LFP batteries less profitable than that of lithium nickel manganese cobalt oxide (NMC) cells.[37] From this aspect, it is essential that second-life applications can make better use of retired LFP cells before they are sent to recycling.[38]

In this work, we collected cycling data of 62 LFP 18650 cells cycled under various operational conditions, such as current, cycle number, etc. Data analytics and Gaussian process modeling were used to predict the cell cycle life given the cycling condition and SoH of early cycles. The non-uniformity in battery cells, such as uneven distributions of active materials, variations of electrode thickness and other manufacturing imperfections, was hypothesized as a reasonable cause of recoverable performance degradation. An equivalent circuit model (ECM) was employed to quantitatively explore the mechanisms of capacity loss and the feasibility of capacity recovery. The experimental reconditioning treatments applied to the aged cells validated their effectiveness with some of the lost capacity recovered. Finally, the importance of different operational parameters to the cell capacity recoverability was assessed by SHapley Additive exPlanations (SHAP) analysis[39], which suggested the significant role of SoH, residual capacity and the cycling current. In this study, we present three key contributions. Firstly, we conducted extensive experiments on the aging and reconditioning of LFP cells on a large scale. These experiments allow us to leverage machine learning models for predicting cycle life. Secondly, we employed an Electrochemical Model (ECM), validated with experimental data, to demonstrate the development of lateral lithium non-uniformity in electrodes. This non-uniformity arises from uneven internal resistance and leads to capacity loss. We also show that such capacity loss can be recovered through the application of extreme voltage holds. Thirdly, we identified crucial parameters influencing the extent of capacity recuperation. Through the reconditioning process, some of the lithium imbalance can be eliminated.

RESULTS AND DISCUSSION

Cycling and SoH assessment

Figure 2(a-l) illustrates the decay curves of discharge capacity concerning cycle number under various currents. The cycle life, defined as the point where cell capacity reaches 1.1 Ah at the end of the first life, corresponding to approximately 73% State of Health (SoH), reveals intriguing insights. Notably, there exist discernible connections between the discharge capacity distribution and the cycling currents applied. Our investigation unveils an interesting observation: the distribution of battery cycle life, under the same cycling current, approximates a Gaussian distribution with symmetrical spreads, as depicted in Figure 2a-II.

Furthermore, when considering discharge capacity, a higher current is associated with a lower mean cycle life and a more tightly clustered distribution. In contrast, a lower current corresponds to a higher mean cycle life and a broader spread. To illustrate, at a cycling current of 3.0 A, the mean cycle life is approximately 100 cycles, with a range spanning from 50 to 200 cycles. Conversely, under a 1.0 A cycling current, the mean cycle life extends to around 900 cycles, encompassing a broader range from 600 to 1400 cycles.

Typical discharge curves and the corresponding relationships of differential capacity (dQ/dV) with respect to cell voltage at 2.0 A and 1.0 A are plotted in Figure 2(b). A larger capacity drop between the 10th and 50th cycles is observed in the cell cycled at a higher current. There are distinctive features in the dQ/dV curves in terms of peak positions and intensities at different currents and cycles. These features provide additional information about degradation compared to the features reported in high-power LFP cells.[15] In addition, Supplemental Information Figure S4 presents the capacity decay and features of charge-discharge curves at different SoHs for a cell cycled at 1.0 A.

Table 1. Summary of the average RMSE and MAPE values for battery cycle life prediction obtained by evaluating the tuned models on the 5 train-validation/test sets, with the average and their standard deviation given as the first, and second number in the cell, respectively.

Models	Mean of 5-fold CV RMSE (cycles)		Mean of 5-fold CV MAPE (%)	
	Train-validation	Test	Train-validation	Test
LR model	155 ± 7	173 ± 26	54.18 ± 2.29	65.07 ± 18.46
GPR model	109 ± 12	145 ± 48	23.77 ± 1.64	39.39 ± 15.80
GBR model	13 ± 1	140 ± 42	5.08 ± 0.45	16.84 ± 1.87

We used data-driven approaches to predict cycle life with both the linear model (LR) and the non-linear models (GPR and GBR). In line with Severson et al.'s study[15], we adopted RMSE and MAPE to assess model performance and generalizability. All the models take as a feature the log variance of the discharge curve difference between cycles n_{start} and n_{end}, represented as $var(\Delta Q_{n_{start}-n_{end}}(U))$ (Supplemental Information Figure S5). Severson et al.'s study[15] has highlighted the predictive power of this variance, alongside the current and the capacity difference, $(\Delta Q_{n_{start}-n_{end}})$, between the two cycles. The cycle number set $(n_{start},\ n_{end})$ is regarded as hyperparameters. While the dataset of 62 cells is relatively large in the academic battery community, it is still relatively small for model fitting and as a result, our data-driven models are prone to overfitting. To reduce overfitting, we implemented nested CV where model generalizability is evaluated in the outer loop while hyperparameter tuning is performed in the inner loop (Supplemental Information Figure S3).

Table 1 shows the average RMSE and MAPE values for battery cycle life prediction obtained by evaluating the tuned models on the 5 train-validation/test sets followed by averaging the RMSE and MAPE values obtained; the standard deviation of each average RMSE or MAPE is also indicated in the table. The LR model reports an average test RMSE of 173 and an average test MAPE of 65.07% across the 5 test sets. These linear models generally perform poorer than the nonlinear models (more details can be found in Supplemental Information Figure S6). Besides linear models, we also explored nonlinear models such as GPR and GBR for cycle life forecasting. Both GPR and GBR models prove to be a better fit for our dataset than the LR models are. The average test RMSEs for the GPR and GBR stand at 145 and 140, respectively (Supplemental Information Figures S7 and S8). In terms of test MAPE, the GBR performs the best with an average test MAPE as low as 16.84% across the 5 test sets.

The grid search for hyperparameters $(n_{start},\ n_{end})$ in the inner loop using CV for all models is detailed in Supplemental Information Figures S6 to S8. The GBR models display some variability in hyperparameters across the inner loop grid search. Figure 2(c) presents an example of the parity plot of cycle life in which the GBR model is tuned and evaluated on the first fold of the outer loop (fold index = 0), which also happens to have the lowest RMSE and MAPE across all 5 outer loop folds. Figure 2(d) provides an example of the contour plot of the validation set RMSE during grid search hyperparameter tuning; in this case, the optimal

(n_{start}, n_{end}) was found to be (19, 77). Despite the variability in hyperparameters across different CV partitions, the GBR model's low test MAPE suggests that data-driven early prediction of the LFP cell's cycle life is feasible with our dataset, agreeing with the conclusion of Severson et al.'s prior study.[15]

Non-uniformity and aging

It is hardly possible to realize perfect uniformities during battery cell manufacturing. As illustrated in Figure 3(a), either non-uniform materials distributions or uneven stacking of electrodes will lead to non-uniform ion transport and current density variations across the electrodes. Upon cycling, electrode materials may experience different volume changes due to the bias current/voltage. The side electrochemical reactions, e.g. SEI formation or Li plating, would be localized at different places on the electrodes as well. Compared with the intact anode and clean separator before cycling (Figure 3b), the photos after cycling (Figure 3c) show detached areas and white materials on the anode. Some dark strips of residual materials are also observed on the separator. It clearly demonstrates regionalized materials degradation and side reactions during the cell operation.

To have a closer examination, top view and cross-sectional view SEM images and elemental mappings of the anode before and after cycling are shown in Figure 3(d) and 3(e). Before cycling, the elemental distributions of carbon (C) and fluorine (F) on the surface (Figure 3d-i) are relatively uniform. The anode layers (~50 µm in thickness) are attached to the current collector well (Figure 3d-ii). In contrast, the C and F distributions on the surface after cycling (Figure 3e-I) indicate that certain F-rich materials form at some areas. The anode layer in Figure 3(e-II) also becomes thicker (~58 µm) and its adhesion with the current collector becomes much worse. The observations of electrode materials at various magnifications confirm that the chemical and structural changes during cycling are uneven. Concurrently, the electric/electrochemical behaviors across the electrode will change differently. During cycling, some places will accumulate a higher potential for electric transport or electrochemical reaction as shown in Figure 4(a-I) and 4(a-II). The electric potential changes are dynamic during battery operation. Although the high potential differences may decrease after resting (Figure

4a-III), especially for high current operations, an electrical reconditioning step is recommended to further redistribute the Li ions, re-homogenize the electric potential differences and recover usable capacity (Figure 4a-IV).

Using the ECM simulation (Figure 4b), we can track the amount of lithium in each sub-cell during cycling (Figure 4c), and reconditioning (Figure 4d), with experiment-extracted model parameters presented in Table 2. More details of the fitting process are provided in the 'ECM Fitting Procedure' section in Supplemental Information Tables S2-S4.

Table 2. Parameters for the used ECM. There are 9 unknown parameters in the ECM (Figure 4B) with their prior ranges list in Supplemental Information Table S4. Following the protocols listed in Supplemental Information Table S2, the simulation results are obtained by applying the global optimization algorithm of differential evolution implemented in the SciPy library.

Parameter	**Value**
$R_1^{\pm}$	149.85 mΩ
$R_2^{\pm}$	88.15 mΩ
R_e	44514.26 mΩ
$R_0 = \left(2k/(k+1)\right)R_2^{\pm}$	111mΩ
$k = R_1^{\pm}/R_2^{\pm}$	1.7
$k_e = R_e/R_2^{\pm}$	505
$U_{OCP,1/2}^{-}\left(z_{1/2}^{-}\right)$	Graphite (MCMB) Open Circuit Potential from Plett (2015).[40] 2.4V to 4.6V for z^{-} from 1 to 0.
$U_{OCP,1/2}^{+}\left(z_{1/2}^{+}\right)$	LFP Open Circuit Potential from Plett (2015).[40] 0.0V to 3.0V for z^{+} from 1 to 0.
Q_{max}^{-}	1.227Ah
$r_{N/P} = Q_{max}^{-}/Q_{max}^{+}$	1.064
$z_1^{-}(t_0)$	0.001
$z_1^{+}(t_0)$	0.752
$z_2^{-}(t_0)$	0.104
$z_2^{+}(t_0)$	0.983

We can clearly see that the lithium in the two sub-cells diverge substantially from each other upon cycling and eventually settle to some steady level (Figure 4c), with sub-cell 1 losing lithium, and sub-cell 2 gaining lithium. These divergences would illustrate the lithium inhomogeneity built up during cycling, by lithium movement across the bridge resistor R_e.

Capacity recuperation

Upon reconditioning, where the cell was held at a constant voltage (3.6 V or 2.0 V), the lithium ions in the two sub-cells are gradually equalized as shown in Figure 4(d). These results suggest that the capacity recovery observed experimentally was contributed by the re-homogenization of Li ions. In addition, the capacity check of the cell at open-circuit resting was also conducted before and after the reconditioning in Supplemental Information Figure S9. There is a relaxation process during transit time, i.e after cycling and before constant voltage reconditioning. This relaxation recovers some of the cell's capacity, which saturates after a period. The constant voltage reconditioning brings back more capacity and the recovered capacity is stable during the following cycles as shown in Supplemental Information Figure S9. This observation reflects the scenario of capacity recovery during open circuit resting and constant voltage reconditioning presented in Figure 4(d).

Electric reconditioning treatments were carried out on the aged LFP cells as described in the experimental section. Various capacities together with recovery rates are defined and demonstrated in Figure 5(a). The ECM can reasonably replicate the charge and discharge curves before and after reconditioning (Figure 5b), with experimentally extracted parameters given in Table 2. The fitting yields $R_e = 44\ \Omega$, which is two orders of magnitude larger than $R_1 = 0.15\ \Omega$ and $R_2 = 0.088\ \Omega$. Tracking the sub-cell lithium content with those parameters, the simulated Li inhomogeneity built-up during cycling is less than experimentally observed (Figure 4c and 4d). This implies that there might be driving forces other than non-uniform resistance that promote the lateral lithium inhomogeneity, which the current ECM model had not considered yet. The ECM model does not incorporate any non-recoverable degradation mechanism which accounts for the substantial capacity fade from the nominal 1.5 Ah to about 1.0 Ah upon cycling. The electrode capacities obtained by parameter fitting also indicate significant loss of active materials and loss of lithium inventory, which may not be laterally uniform, and could also contribute to the observed lithium inhomogeneity. Despite these limitations, this simple ECM demonstrates the possibility of lithium non-uniformity build-up due to resistance difference and provides a mechanistic explanation for how inhomogeneous lithium can reduce the apparent capacity and how such capacity loss can be recovered by extreme voltage hold.

Reconditioning recovered between 0.02 Ah to 0.21 Ah, which translates to 3-34% recovery of the loss capacity (Figure 5c-I and -II). There is a negative correlation between the residual capacity C_{res} and the recovered capacity C_{rec} (Figure 5c-I), as higher cycling rates seems to recover more (i.e 2.0 A and 3.0 A) than those that cycled with lower rates (i.e 1.0 A and 1.5 A). In general, the recovery metrics (C_{rec}, r_1) increase with loss in capacity (lower residual capacity C_{res}) (Figure 5c). This is more prominent with r_1, which has a negative linear correlation with C_{res}. On the other hand, the relationship between C_{res} and r_2 is complex. There is a negative correlation for cells that are cycled with 1.0-2.0 A current, but a positive correlation for cells that are cycled with 3.0 A current. Cycling with 3.0 A (~2C) current can be considered harsh, so we would expect it to decrease the recoverable capacity. However, some cells from the high cycling rate showed relatively high r_2 recovery rates (Figure 5c-III).

The results for other parameters, like the initial capacity $C_{init} = C_{res} + C_l$, SoH and cycle number (#), are provided in Supplemental Information Figure S10. Furthermore, the capacity decay curves display knee points, indicating a rapid decline in capacity in subsequent cycles. To investigate the relationship between recovery capacity and knee points, we extracted cycle numbers around these knee points and plotted them against recovery capacity (C_{rec}) and recovery rates (r_1 and r_2) for cells cycled at 2.0 A (Supplemental Information Figure S11). The cycle numbers at knee points are determined by "Tangent ratio" method.[12] Our analysis revealed that the associations between cycle numbers at knee points and recovery capacities/rates are highly varied, suggesting that the occurrence of knee points is less predictable based on recovery capacities.

Overall cell capacity recoverability can be well predicted from the cycling parameters (current and number of cycles) and states of the cells (C_{init}, SoH, C_{res}). Here, a linear regression model performs very well in predicting the cell's recoverability in terms of the recovery rate r_1 (Figure 5d). Prediction of other recovery indicators C_{rec}, and r_2 also works well with a linear regression model (Supplemental Information Figure S12). In Figure 5(e), SHAP[39] analysis showed that SoH is the most important parameter to affect C_{rec}, r_1 and r_2. More details of their correlations are given in Supplemental Information Figure S13. In the case where the history of cycling is unknown, r_1 seems to be the best metric to estimate the cell's capacity recoverability. r_1 correlates well linearly with SoH (Supplemental Information Figure S10) and is reasonably less sensitive to cycling rates.

Conclusions

Data-driven health estimation and statistical analysis of capacity recovery of aged Li-ion batteries play significant roles in their second-life applications. Machine learning modeling on our cycling dataset of 62 LFP/graphite 18650 cells showed that it is possible to make early prediction of cell cycle life. A gradient boosting regression model is used to demonstrate the feasibility of early prediction of battery cycle life with a test RMSE of 140 $\pm$ 42 cycles and test MAPE of 16.84% $\pm$ 1.87%, using data from the first 80 cycles. Non-uniformities are detected in battery cells, which are proposed as a reason for performance degradation and capacity loss. The equivalent circuit model simulation suggests lateral lithium inhomogeneity can build up upon cycling due to uneven internal resistance, while such inhomogeneity contributes to apparent capacity loss. The simulation also indicates that extreme voltage hold can be effective in re-homogenizing lithium and recovering the portion of lost capacity caused by lithium inhomogeneity. Recuperation effectiveness is validated by reconditioning experiments with considerable capacity recovery rates at different conditions. Further data analysis reveals the importance of SoH in determining the capacity recovery of aged LFP batteries. This study demonstrates the promising applications of data-driven methods and equivalent circuit modeling in battery diagnostics and highlights their significance in the emerging field of second-life batteries.

EXPERIMENTAL PROCEDURES

Battery cycling

Commercially available LFP/graphite 18650 cells with a nominal capacity of ~1.5 Ah (high-energy type) were used in this study. This type of cells has a higher capacity but shorter cycle life in contrast to the LFP 18650 cells used in a previous study (high-power type) by Severson et al. Even for the same LFP chemistry, more comprehensive data from diverse cells are helpful for developing robust data-driven methodologies and understanding cell inconsistencies. Constant current charge and constant current discharge cycling with a voltage window from 2.5 V to 4.0 V was applied to perform cell aging. The charge-discharge current was varied at 1.0 A, 1.5 A, 2.0 A and 3.0 A to investigate its effects on cell aging and recovery. The testing was carried out on a 16-channel battery tester (Maccor, Model-4200) in ambient environment. The photos of battery cells and testing setup are presented in Supplemental Information Figure S1. The details of cell cycling information are listed in Supplemental Information Table S1.

Capacity recuperation

The accumulated non-uniform distribution of lithium ions upon cycling is believed to be one of the causes of the capacity fade. The non-uniform Li distributions would result in significant potential gradients, when the voltage of a cell has a big slope. A reconditioning process with an applied potential across the electrodes could drive and re-distribute the ions more uniformly. For LFP/Graphite cells, large voltage gradients appear around fully charged (100% SoC) and fully discharged (0% SoC). Accordingly, the voltage values at 100% SoC (3.6 V) and 0% SoC (2.0 V) are chosen as applied potentials for the reconditioning treatments. A previous study also shows a reconditioning period of 72 h (3 days) is able to reach a relatively stable state for LFP cells,[35] so the holding time is kept at 72 h in this work. This procedure was applied to all the cells with different aging histories. The cell capacities before and after the treatments were checked by cycles of a constant current charge and a constant current discharge at a small current of 0.3 A. Typical voltage and current curves of the recuperation and capacity check processes are shown in the Supplemental Information Figure S2. The recovery rates were calculated as the ratio of recovered capacity to both the residual and lost capacity.

Data-driven assessment of battery states

The discharge capacity data were batch processed to build the distributions of the cycle life. We set the discharge capacity of 1.1 Ah as the cutoff value at end of first life to define the cycle life for an acceptable SoH around 73% (1.1 Ah/1.5 Ah) for the cells (Figure 2a). We consider several combinations of features to build a model to predict cycle life, which are the number of cycles to reach a discharge capacity of 1.1 Ah, the cycling current, two early discharge capacities at 'start' cycle number n_{start} and 'end' cycle number n_{end}, and variance of discharge curve difference between two cycles $var(\Delta Q(U))$.[15]

We employed three regression models—linear regressor (LR), Gaussian process regressor (GPR), and gradient boosting regressor (GBR)[41] —to forecast the cycle life across our dataset comprising 62 cells. Although this dataset size is relatively substantial within the academic battery community, it is deemed small for effectively fitting machine learning models, making them susceptible to overfitting. To mitigate overfitting, a common issue in data-driven models trained on limited datasets, we conducted nested cross-validation (CV). This process involves an outer loop for assessing test errors and an inner loop for hyperparameter tuning, illustrated in Supplemental Information Figure S3. The outer CV loop divides the data into five sets of train-validation and test sets, indexed from 0 to 4 (see Supplemental Information Figure S3). Simultaneously, the inner CV loop further divides each train-validation set into five sets of train and validation sets, utilized for hyperparameter tuning.

For hyperparameter tuning, a grid search was conducted within the inner loop over the $(n_{start},\ n_{end})$ hyperparameters to reduce the mean square error (MSE) on the validation set. An optimal set of $(n_{start},\ n_{end})$ from this inner loop hyperparameter tuning is selected such that it gives the lowest average MSE on the 5 inner loop validation sets. Using this optimal set of $(n_{start},\ n_{end})$, the model is finally retrained on the train-validation set. At the end of the entire nested CV campaign, we had 5 tuned models that correspond to the 5 train-validation/test sets in the outer loop. The final model performance is quantified by the average of the 5 root mean square errors (RMSEs) and the average of 5 mean absolute percentage errors (MAPEs) evaluated on the train-validation and test sets. These test error metrics provide an estimate of the generalization performance of the model in predicting cycle life.

Simulation of capacity loss and recovery using equivalent circuit modeling

Lateral electrode inhomogeneity of lithium-ion cells has been widely studied in literature to better understand its causes and characteristics.[35] Such inhomogeneity has been attributed to manufacturing variations and defects, certain cell form factors, and tab locations, which in turn give rise to a non-uniform current density and hence uneven lithium ion distribution. Some efforts have also focused on simulating the formation of such a inhomogeneity using physics-based and circuit-based models[42], by dividing a cell laterally into multiple local mini-cells and accounting for the internal resistance associated with the interconnection among these mini-cells. However, there is little work that studies how such inhomogeneity affects the usable capacity, and how capacity loss due to inhomogeneity may be recovered by homogenizing the cell using certain operations.

Spingler and coworkers[35] proposed that shallow cycling around the mid state-of-charge (SOC) range with shallow electrode open circuit voltage (OCV) curves can significantly encourage inhomogeneity to develop and reduce usable capacity within a voltage window. They also showed experimentally that capacity loss can be recovered by holding the cell for several days at extreme voltage at which the electrode OCV curves are much steeper. They proposed that such a phenomenon might be captured by an ECM but have not implemented and tested this idea. In this work, we implement a simple ECM to simulate the recoverable capacity loss due to lithium inhomogeneity and its recovery under extreme voltage reconditioning, and we compare the simulation results to experimental measurements.

To demonstrate the formation of lithium inhomogeneity and the effects of electric reconditioning on the capacity recovery of aged LFP batteries, an ECM simulation is carried out. We divide the cell laterally into two parallel sub-cells of equal capacity. For each sub-cell, we model the anode and cathode open circuit potential separately ($U_{OCV,1}$, $U_{OCV,2}$). This contrasts with the monolithic full-cell OCV used by most ECMs in literature. Moreover, we associate an internal resistance (R_1, R_2) with each electrode and add a bridge connecting the two sub-cells that accounts for the electrolyte resistance (R_e), which lithium ions need to overcome to transport laterally across different sub-cells. This bridge R_e is what enables the lithium distribution to become uneven when one sub-cell somehow has lower resistance

($R_2^{\pm} < R_1^{\pm}$), so lithium ions may prefer to be cycled within that branch, driving the lateral transport through the bridge. Since the electrodes are manufactured to be thin but with a large cross-section to minimize internal resistance while maintaining substantial capacity, the lateral resistance R_e at the bridge is typically much larger than the thickness-wise resistances ($R_1^{\pm}$ and $R_2^{\pm}$). This ECM is the most parsimonious model that can simulate the effects of lateral lithium inhomogeneity.

To find suitable values for the ECM parameters (R_1, R_2 and R_e), we fit the ECM to the experimental cell terminal voltage curves for the last few cycles and the whole recuperation process, including capacity checkup steps. We solve this nonlinear least squares problem using the differential evolution algorithm as implemented in the Python library SciPy.[43]

Capacity recovery statistics

In this section we are interested in quantifying the recoverable capacity, as well as the factors that contribute to the cell's capacity recoverability. We define several metrics to quantify the recovery rate, namely residual capacity (C_{res}), lost capacity (C_l), capacity after reconditioning (C_{aft}) and recovered capacity (C_{rec}). Here, we take the capacity value after cycling for C_{res}, which is slightly different from the capacity prior to reconditioning. In this case, C_{rec} has accounted for capacity increase during the transition time between the end of cycling and reconditioning.

Furthermore, we also define two different parameters to quantify the capacity recovery rate, $r_1 = \frac{C_{rec}}{C_{res}} \times 100$ and $r_2 = \frac{C_{rec}}{C_l} \times 100$. r_1 would quantify the effect of residual capacity C_{res} on the recoverable capacity. In contrast, r_2 quantifies the portion of lost capacity that is recovered. We used SHAP analysis[39] to quantify the importance of recovery parameters.

SUPPLEMENTAL INFORMATION

Supplemental Information can be found online at …

ACKNOWLEDGEMENT

This research is supported by A*STAR (project no. C210812038) and EMA-EP011-SLEP-001 (SC25/21-708712). R.I.M. acknowledges funding from Accelerated Materials Development for Manufacturing Program at A*STAR via the AME Programmatic Fund by the Agency for Science, Technology and Research under Grant (Project Code A188b0043), IAF-PP grant number M22K8a0048 (SC25/23-833412). J.L., Y.Z. and E.K. acknowledge funding by Agency for Science, Technology and Research (A*STAR) under the Career Development Fund (C210112037). The authors acknowledge Dr. Kedar Hippalgaonkar and Dr. D. V. Maheswar Repaka for helpful discussion during project initiation.

AUTHOR CONTRIBUTIONS

G.Z., X.Y. and E.K. conceived the concept. X.Y., J.Z., L.C.H.M, Z.L. and N.D. conducted the experiments on battery testing and characterization. R.I.M. and Y.Z. performed machine learning and data analytics. J.L. helped with the equivalent circuit modeling and simulation. R.I.M., J.L., Y.Z., S.Y.C, E.K. and X.Y wrote the paper. All authors helped to revise the manuscript.

DECLARATION OF INTERESTS

The authors declare no competing interests.

REFERENCES

1. Zhou, Y., Gohlke, D., Rush, L., Kelly, J., and Dai, Q. (2021). Lithium-ion battery supply chain for E-drive vehicles in the United States: 2010–2020. Argonne National Lab.(ANL), Argonne, IL (United States). https://doi.org/10.2172/1778934
2. Morse, I. (2021). A dead battery dilemma. Science *372*, 780-783.
3. Lander, L., Cleaver, T., Rajaeifar, M.A., Nguyen-Tien, V., Elliott, R.J., Heidrich, O., Kendrick, E., Edge, J.S., and Offer, G. (2021). Financial viability of electric vehicle lithium-ion battery recycling. Iscience *24*, 102787.
4. Harper, G., Sommerville, R., Kendrick, E., Driscoll, L., Slater, P., Stolkin, R., Walton, A.,

Christensen, P., Heidrich, O., and Lambert, S. (2019). Recycling lithium-ion batteries from electric vehicles. Nature *575*, 75-86.

5. (2019). Recycle spent batteries. Nat. Energy *4*, 253-253. https://doi.org/10.1038/s41560-019-0376-4
6. Mao, J., Ye, C., Zhang, S., Xie, F., Zeng, R., Davey, K., Guo, Z., and Qiao, S. (2022). Toward practical lithium-ion battery recycling: adding value, tackling circularity and recycling-oriented design. Energy Environ. Sci. *15*, 2732-2752.
7. Baars, J., Domenech, T., Bleischwitz, R., Melin, H.E., and Heidrich, O. (2021). Circular economy strategies for electric vehicle batteries reduce reliance on raw materials. Nat. Sustain. *4*, 71-79.
8. Chen, M., Ma, X., Chen, B., Arsenault, R., Karlson, P., Simon, N., and Wang, Y. (2019). Recycling end-of-life electric vehicle lithium-ion batteries. Joule *3*, 2622-2646.
9. Zhu, J., Mathews, I., Ren, D., Li, W., Cogswell, D., Xing, B., Sedlatschek, T., Kantareddy, S.N.R., Yi, M., and Gao, T. (2021). End-of-life or second-life options for retired electric vehicle batteries. Cell Rep. Phys. Sci. *2*, 100537.
10. Engel, H., Hertzke, P., and Siccardo, G. (2019). Second-life EV batteries: The newest value pool in energy storage. McKinsey & Company.
11. Hossain, E., Murtaugh, D., Mody, J., Faruque, H.M.R., Sunny, M.S.H., and Mohammad, N. (2019). A comprehensive review on second-life batteries: Current state, manufacturing considerations, applications, impacts, barriers & potential solutions, business strategies, and policies. IEEE Access *7*, 73215-73252.
12. Attia, P.M., Bills, A., Planella, F.B., Dechent, P., Dos Reis, G., Dubarry, M., Gasper, P., Gilchrist, R., Greenbank, S., and Howey, D. (2022). “Knees” in lithium-ion battery aging trajectories. J. Electrochem. Soc. *169*, 060517.
13. Hu, X., Xu, L., Lin, X., and Pecht, M. (2020). Battery lifetime prognostics. Joule *4*, 310-346.
14. Yi, Z., Chen, Z., Yin, K., Wang, L., and Wang, K. (2023). Sensing as the key to the safety and sustainability of new energy storage devices. Prot. Control Mod. Power Syst. *8*, 1-22.
15. Severson, K.A., Attia, P.M., Jin, N., Perkins, N., Jiang, B., Yang, Z., Chen, M.H., Aykol, M., Herring, P.K., and Fraggedakis, D. (2019). Data-driven prediction of battery cycle life before capacity degradation. Nat. Energy *4*, 383-391.
16. Roman, D., Saxena, S., Robu, V., Pecht, M., and Flynn, D. (2021). Machine learning pipeline for battery state-of-health estimation. Nat. Mach. Intell. *3*, 447-456.
17. Li, W., Sengupta, N., Dechent, P., Howey, D., Annaswamy, A., and Sauer, D.U. (2021). Online capacity estimation of lithium-ion batteries with deep long short-term memory networks. J. Power sources *482*, 228863.
18. Aitio, A., and Howey, D.A. (2021). Predicting battery end of life from solar off-grid system field data using machine learning. Joule *5*, 3204-3220.
19. Takahashi, A., Allam, A., and Onori, S. (2023). Evaluating the feasibility of batteries for second-life applications using machine learning. iScience *26,* 106547.
20. Xu, Q., Wu, M., Khoo, E., Chen, Z., and Li, X. (2023). A hybrid ensemble deep learning approach for early prediction of battery remaining useful life. IEEE/CAA J. Autom. Sin. *10*, 177-187.
21. Ma, N., Yin, H., and Wang, K. (2023). Prediction of the remaining useful life of supercapacitors at different temperatures based on improved long short-term memory. Energies *16*, 5240.
22. Jiang, B., Gent, W.E., Mohr, F., Das, S., Berliner, M.D., Forsuelo, M., Zhao, H., Attia, P.M., Grover, A., and Herring, P.K. (2021). Bayesian learning for rapid prediction of lithium-ion battery-cycling

protocols. Joule *5*, 3187-3203.

23. Weng, A., Mohtat, P., Attia, P.M., Sulzer, V., Lee, S., Less, G., and Stefanopoulou, A. (2021). Predicting the impact of formation protocols on battery lifetime immediately after manufacturing. Joule *5*, 2971-2992.
24. Liu, Y., Wang, L., Li, D., and Wang, K. (2023). State-of-health estimation of lithium-ion batteries based on electrochemical impedance spectroscopy: a review. Prot. Control Mod. Power Syst. *8*, 1-17.
25. Hua, Y., Zhou, S., Cui, H., Liu, X., Zhang, C., Xu, X., Ling, H., and Yang, S. (2020). A comprehensive review on inconsistency and equalization technology of lithium‐ion battery for electric vehicles. Int. J. Energy Res. *44*, 11059-11087.
26. Wang, L., Qiu, J., Wang, X., Chen, L., Cao, G., Wang, J., Zhang, H., and He, X. (2022). Insights for understanding multiscale degradation of LiFePO4 cathodes. eScience *2*, 125-137.
27. Simolka, M., Heger, J.-F., Traub, N., Kaess, H., and Friedrich, K.A. (2020). Influence of cycling profile, depth of discharge and temperature on commercial LFP/C cell ageing: cell level analysis with ICA, DVA and OCV measurements. J. Electrochem. Soc. *167*, 110502.
28. Atalay, S., Sheikh, M., Mariani, A., Merla, Y., Bower, E., and Widanage, W.D. (2020). Theory of battery ageing in a lithium-ion battery: Capacity fade, nonlinear ageing and lifetime prediction. J. Power Sources *478*, 229026.
29. Cui, Y., Du, C., Gao, Y., Yang, J., Zhang, L., Guan, T., Yang, L., Cheng, X., Zuo, P., and Ma, Y. (2016). Recovery strategy and mechanism of aged lithium ion batteries after shallow depth of discharge at elevated temperature. ACS Appl. Mater. Interfaces *8*, 5234-5242.
30. Wang, J., Soukiazian, S., Verbrugge, M., Tataria, H., Coates, D., Hall, D., and Liu, P. (2011). Active lithium replenishment to extend the life of a cell employing carbon and iron phosphate electrodes. J. Power Sources *196*, 5966-5969.
31. Taniyama, K., Kazunori, H., and Shimoyama, K. (2016). Lithium-ion battery capacity recovery method. Patent (EP2688134A1).
32. Palacín, M.R. (2018). Understanding ageing in Li-ion batteries: a chemical issue. Chem. Soc. Rev. *47*, 4924-4933.
33. Waldmann, T., and Wohlfahrt-Mehrens, M. (2017). Effects of rest time after Li plating on safety behavior-ARC tests with commercial high-energy 18650 Li-ion cells. Electrochim. Acta *230*, 454-460.
34. Hall, J.C. (2006). Method for prolonging the life of lithium ion batteries. Patent (US20050127875A1).
35. Spingler, F.B., Naumann, M., and Jossen, A. (2020). Capacity recovery effect in commercial LiFePO4/graphite cells. J. Electrochem. Soc. *167*, 040526.
36. Yang, X.-G., Liu, T., and Wang, C.-Y. (2021). Thermally modulated lithium iron phosphate batteries for mass-market electric vehicles. Nat. Energy *6*, 176-185.
37. Sommerville, R., Zhu, P., Rajaeifar, M.A., Heidrich, O., Goodship, V., and Kendrick, E. (2021). A qualitative assessment of lithium ion battery recycling processes. Resour. Conserv. Recycl. *165*, 105219.
38. Wang, M., Liu, K., Dutta, S., Alessi, D.S., Rinklebe, J., Ok, Y.S., and Tsang, D.C. (2022). Recycling of lithium iron phosphate batteries: Status, technologies, challenges, and prospects. Renew. Sust. Energ. Rev. *163*, 112515.
39. Lundberg, S.M., and Lee, S.-I. (2017). A unified approach to interpreting model predictions.

Advances in Neural Information Processing Systems (NIPS) *30*.

40. Plett, G.L. (2015). Battery management systems, Volume I: Battery modeling (Artech House).
41. Pedregosa, F., Varoquaux, G., Gramfort, A., Michel, V., Thirion, B., Grisel, O., Blondel, M., Prettenhofer, P., Weiss, R., and Dubourg, V. (2011). Scikit-learn: Machine learning in Python. J. Mach. Learn. Res. *12*, 2825-2830.
42. Liu, Y., Zhang, C., Jiang, J., Zhang, L., Zhang, W., Lao, L., and Yang, S. (2023). A 3D distributed circuit-electrochemical model for the inner inhomogeneity of lithium-ion battery. Appl. Energy *331*, 120390.
43. Virtanen, P., Gommers, R., Oliphant, T.E., Haberland, M., Reddy, T., Cournapeau, D., Burovski, E., Peterson, P., Weckesser, W., and Bright, J. (2020). SciPy 1.0: fundamental algorithms for scientific computing in Python. Nat. Methods *17*, 261-272.

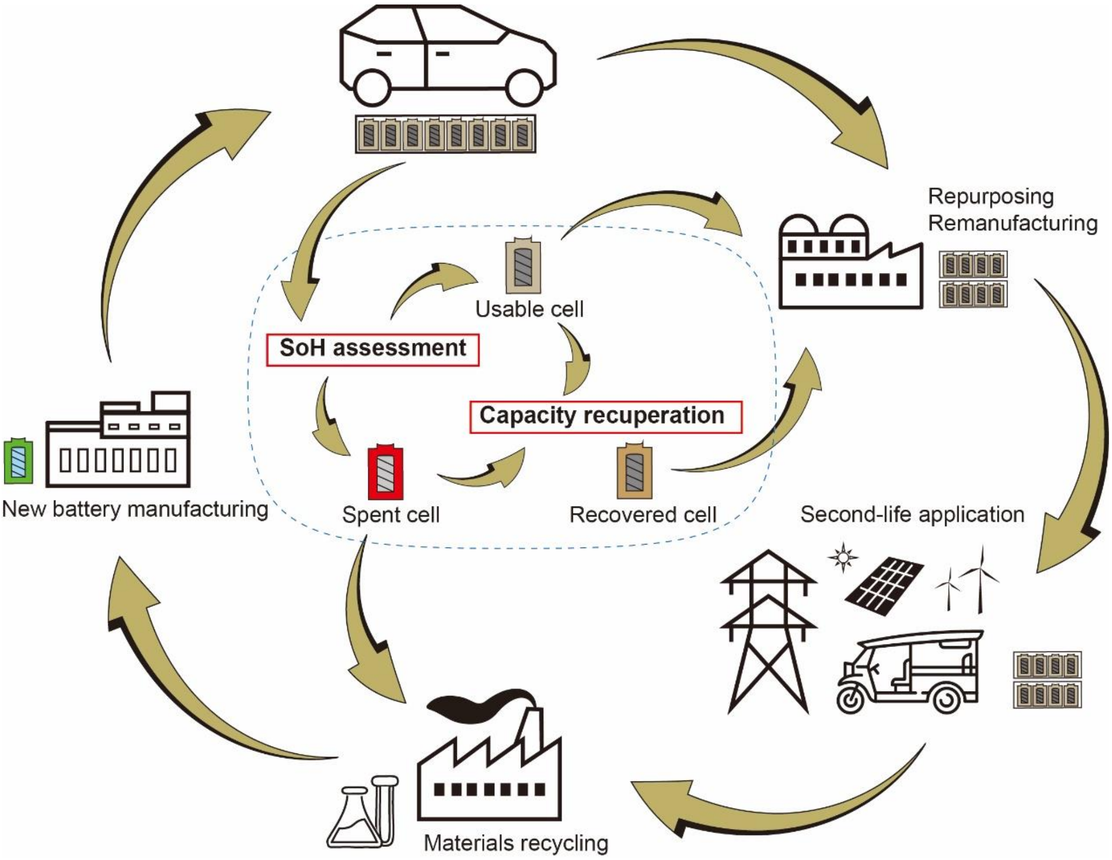

Figure 1. Circular utilization of Li-ion batteries with emphasis on state of health (SoH) assessment and capacity recuperation for second-life applications. The SoH assessment and capacity recuperation play a crucial role in sorting and making better use of retired EV batteries. Those cells with higher residual or recovered capacities can be repurposed to make stationary energy storage systems or less rigorous e-mobilities, like two/three wheelers. For those heavily degraded cells with less usable capacities, they can be directly subjected to recycling to extract raw materials for new cell fabrications.

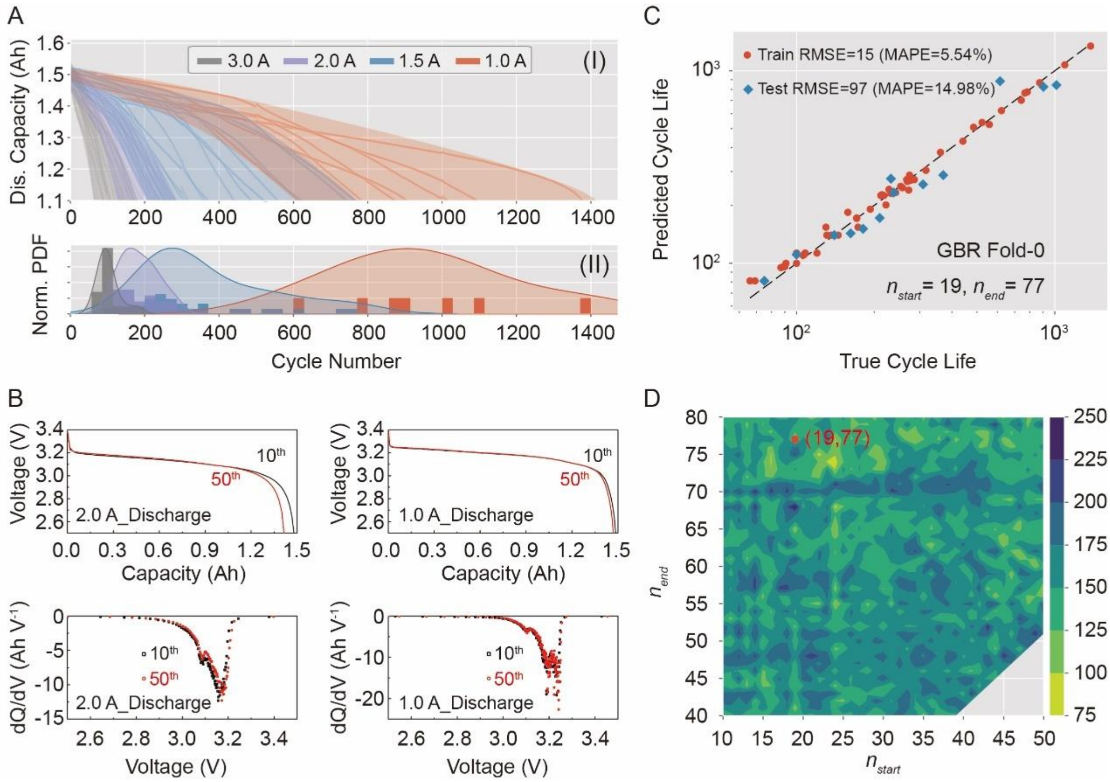

Figure 2. Cycle aging of LFP/graphite 18650 cells and data-driven cycle life prediction.

(A-I) Discharge capacities at various cycling currents (3.0 A, 2.0 A, 1.5 A and 1.0 A). (A-II) Kernel density distribution plots of cycle numbers at a cut-off discharge capacity of 1.1 Ah (defined to be end of first life) for different cycling currents.

(B) Typical discharge and differential capacity (dQ/dV) curves of the 10th and 50th cycles at 2.0 A and 1.0 A.

(C) Example of parity plot of cycle life for a gradient boosting regression (GBR) model that is tuned and evaluated on the first fold of the outer loop, which also happens to give the lowest test RMSE and MAPE across all 5 outer loop folds.

(D) Contour map of the validation set RMSE during grid search hyperparameter tuning, with the optimal hyperparameters (n_{start}, n_{end}) = (19, 77) marked by a red circle. Results from other splits are given in Supplemental Information Figures. S6 to S8.

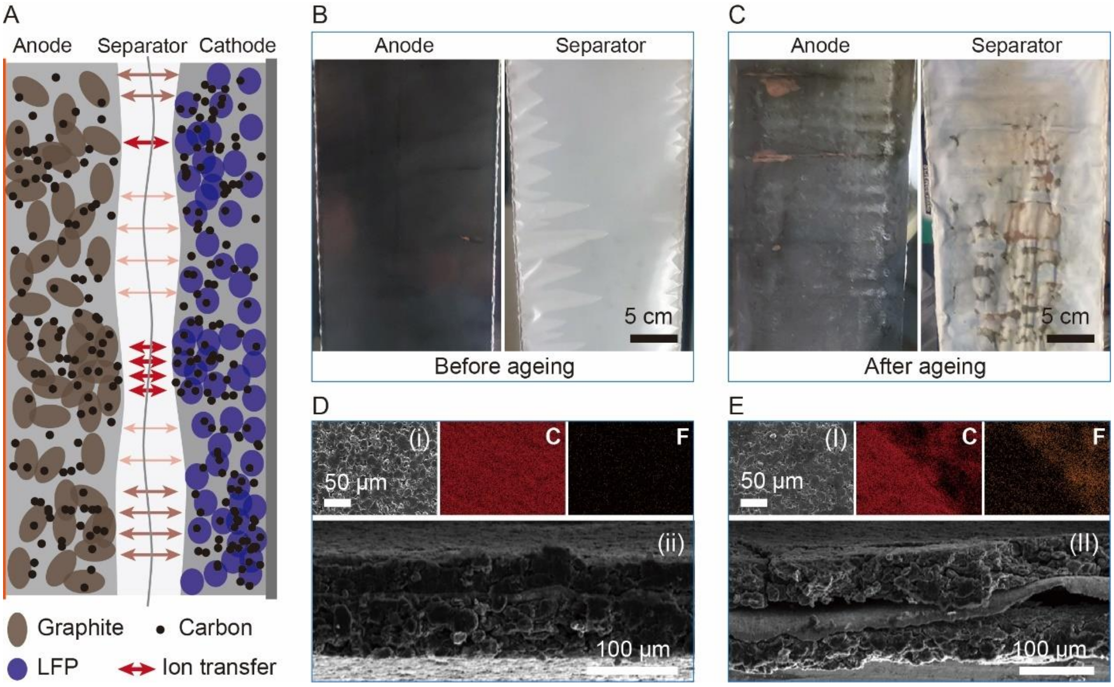

Figure 3. Non-uniformities in battery electrodes before and after cycling.

(A) Illustration of non-uniformities of electrodes and variations of localized ion transfer in LFP/graphite cells.

(B) Optical images of graphite anode and separator before cycle aging.

(C) Optical images of graphite anode and separator after cycle aging.

(D) Top view SEM images (i and I) and elemental mappings of carbon (C) and fluorine (F), and cross-sectional view SEM images (ii and II) of graphite electrodes before cycle aging.

(E) Top view SEM images (i and I) and elemental mappings of carbon (C) and fluorine (F), and cross-sectional view SEM images (ii and II) of graphite electrodes after cycle aging.

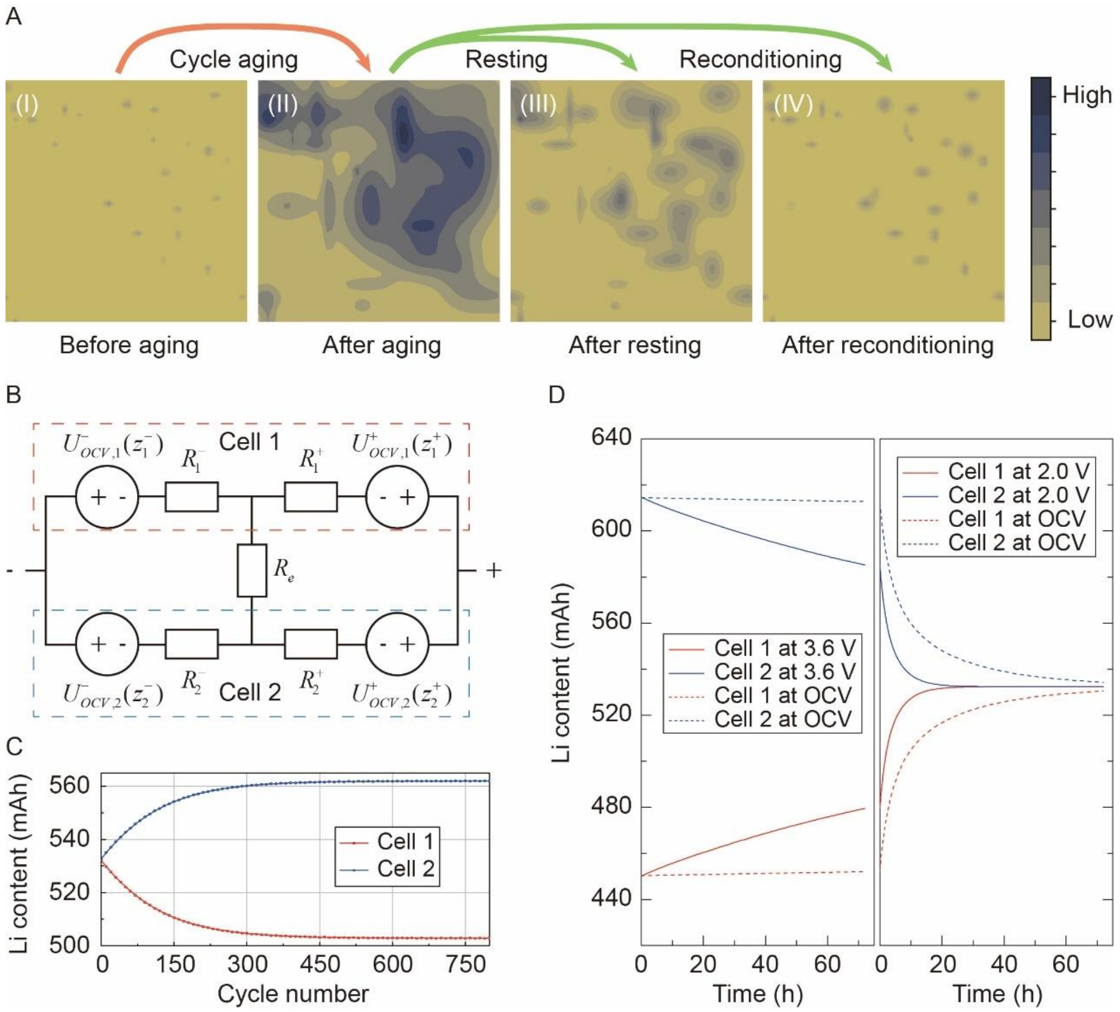

Figure 4. Equivalent circuit modelling of non-uniform lithium distribution during aging and reconditioning.

(A) Schematic demonstration of non-uniform electric potential distribution before (I) and after (II) cycling and corresponding to resting (III) and reconditioning (IV).

(B) Diagram of the equivalent circuit model (ECM).

(C) Plots of time evolution of the amount of lithium in each sub-cell during cycling.

(D) Lithium re-homogenization by holding the cell at constant voltage of 3.6 V (left) and 2.0 V (right). Re-homogenization by open circuit resting is shown by the dashed lines.

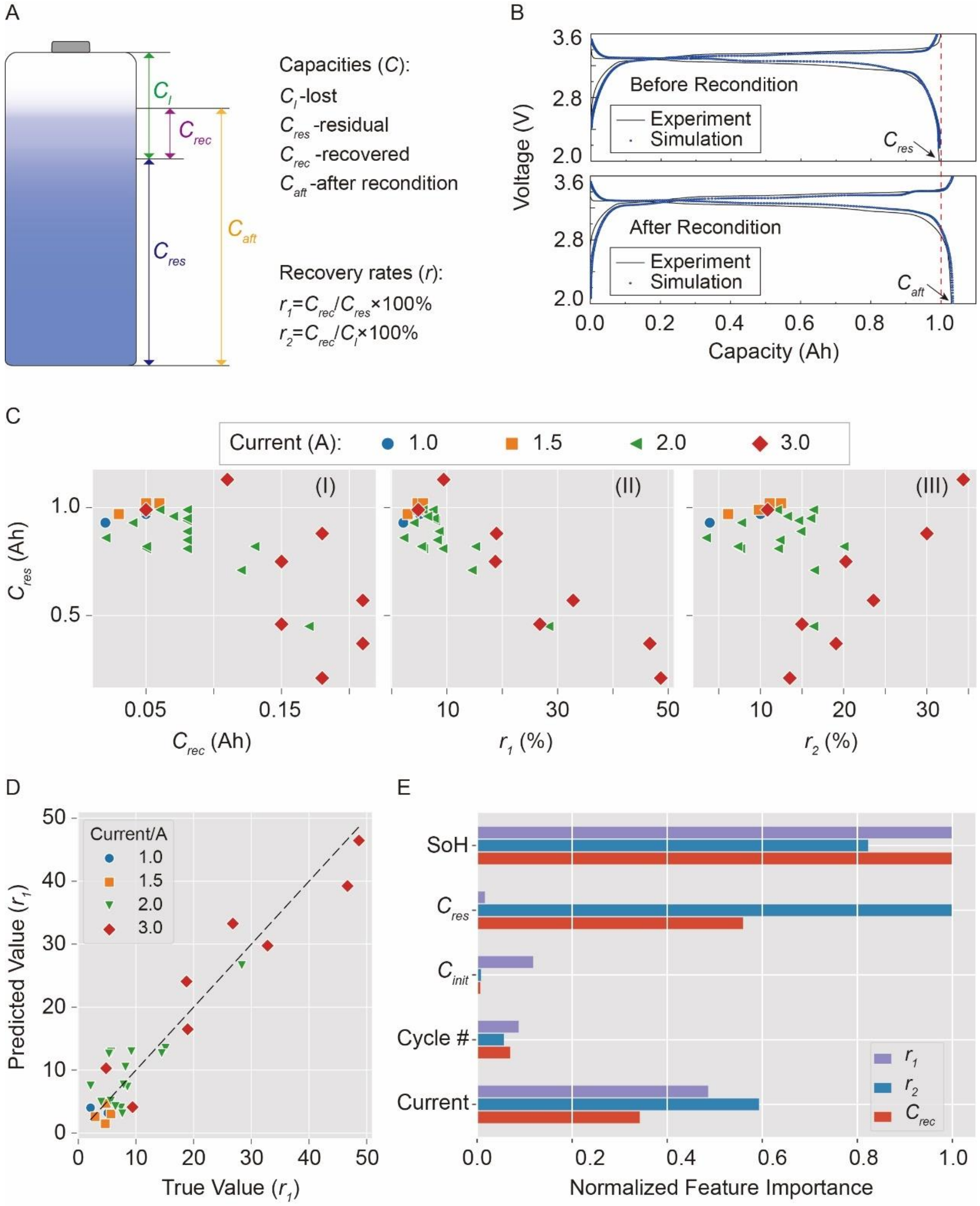

Figure 5. Capacity recovery of aged LFP cells and statistical analyses.

(A) Illustration of various capacities and recovery rates during cell cycling and recuperation operation.

(B) Experimental and simulated voltage profiles of capacity check before and after reconditioning.

(C) Correlation of residual capacity (C_{res}) with respect to recovered capacity (C_{rec}) and recovery rates (r_1 and r_2).

(D) Parity plot of observed and predicted recovery rates r_1 using a linear regression model.

(E) Bar graph showing the importance of different parameters (SoH, C_{res}, C_{init}, Cycle # and Current) for predicting the capacity recovery effects.